AGU PUBLICATIONS

JGR

Journal of Geophysical Research: Space Physics

RESEARCH ARTICLE
10.1002/2015JA021514

Key Points:
- Instability regime transition: from ion Bernstein dispersion to fast magnetosonic dispersion
- Unstable waves follow cold plasma fast magnetosonic dispersion for small concentration of the shell
- Equatorial noise is a subset of more general ion Bernstein waves

Supporting Information:
- Supporting Information S1
- Figure S1
- Figure S2
- Figure S3

Correspondence to:
K. Min,
kmin@auburn.edu

Citation:
Min, K., and K. Liu (2015), Regime transition of ion Bernstein instability driven by ion shell velocity distributions, *J. Geophys. Res. Space Physics*, *120*, 8448–8454, doi:10.1002/2015JA021514.

Received 29 MAY 2015
Accepted 18 SEP 2015
Accepted article online 21 SEP 2015
Published online 10 OCT 2015

Regime transition of ion Bernstein instability driven by ion shell velocity distributions

Kyungguk Min[1] and Kaijun Liu[1]

[1]Department of Physics, Auburn University, Auburn, Alabama, USA

Abstract Linear kinetic dispersion theory is used to investigate a regime transition of the ion Bernstein instability driven by a proton velocity distribution with positive slopes with respect to the perpendicular velocity, $\partial f_p(v_\parallel \sim 0, v_\perp)/\partial v_\perp > 0$. The unstable waves arising from this instability are ion Bernstein waves with proton cyclotron harmonic dispersion. However, in the inner magnetosphere, particularly inside of the plasmapause where plasmas are dominated by a cold background, the instability leads to ion Bernstein waves which approximately follow the cold plasma dispersion relation for fast magnetosonic waves and are, therefore, fast magnetosonic-like. Subsequently, the relevant waves have been termed fast magnetosonic waves and many studies have assumed the cold plasma dispersion relation to describe them. On the other hand, how the dispersion properties of ion Bernstein waves become fast magnetosonic-like has not yet been well understood. To examine this regime transition of the instability, we perform linear dispersion analyses using a two-component proton model of $f_p(\mathbf{v}) = f_M(\mathbf{v}) + f_s(\mathbf{v})$, where f_M is a Maxwellian velocity distribution and f_s is an isotropic shell velocity distribution. The results show that the unstable waves are essentially ion Bernstein waves; however, when the shell proton concentration becomes sufficiently small (less than 10%), the unstable waves approach the cold plasma dispersion relation for fast magnetosonic waves and become fast magnetosonic-like. Although a reduced proton-to-electron mass ratio of 100 has been used for convenience, which reduces the number of unstable modes involved by lowering the lower hybrid frequency, this does not change the overall regime transition picture revealed in this study.

1. Introduction

Originally called "equatorial noise" [*Russell et al.*, 1970], enhanced electric and magnetic field fluctuations with a series of spectral peaks spaced at multiples of the proton cyclotron frequency up to the lower hybrid frequency have been observed within a few degrees of the geomagnetic equator between 2 and 8 R_E [*Russell et al.*, 1970; *Perraut et al.*, 1982; *Santolík et al.*, 2002; *Meredith et al.*, 2008; *Ma et al.*, 2013; *Balikhin et al.*, 2015]. These waves are driven by tenuous energetic proton velocity distributions with $\partial f_p(v_\parallel \sim 0, v_\perp)/\partial v_\perp > 0$, where $f_p(v_\parallel, v_\perp)$ is the proton velocity distribution function and $v_\parallel$ ($v_\perp$) denotes the velocity parallel (perpendicular) to the background magnetic field [*Horne et al.*, 2000; *Chen et al.*, 2010]. In the inner magnetosphere, especially within the plasmapause, these energetic protons are often immersed in a dense cold background plasma [*Chen et al.*, 2011; *Thomsen et al.*, 2011; *Ma et al.*, 2014]. Wave growth then occurs close to the oblique whistler mode/fast magnetosonic mode branch of the cold plasma dispersion relation (referred to as cold plasma magnetosonic dispersion hereinafter) with phase speeds (v_{ph}), especially at low harmonic frequencies, close to the Alfvén speed (v_A) [*Gul'elmi et al.*, 1975; *Perraut et al.*, 1982; *McClements et al.*, 1994; *Horne et al.*, 2000; *Chen et al.*, 2010]. Using the same parameters as in *Horne et al.* [2000], *Chen* [2015] presented a warm plasma solution of fast magnetosonic waves (Figure 1 therein), showing that the dispersion relation is very close to the cold plasma magnetosonic dispersion relation. Thus, the relevant waves have more recently been termed "fast magnetosonic waves."

In situations different from those found in the inner magnetosphere, the unstable waves driven by proton velocity distributions with $\partial f_p(v_\parallel \sim 0, v_\perp)/\partial v_\perp > 0$ are more generally described as ion Bernstein waves which exhibit proton cyclotron harmonic dispersion as Bernstein modes, but do not necessarily follow the cold plasma magnetosonic dispersion relation [*Gary et al.*, 2010, 2011]. Using a simple model, *Perraut et al.* [1982] suggested that more intense rings with a smaller ring speed than the Alfvén speed in the nightside injection region can excite waves with phase speed substantially less than the Alfvén speed. *Janhunen et al.* [2003]

showed that the ion shell distribution observed in the ionosphere where plasma beta is usually very small can excite ion Bernstein waves which are predominantly electrostatic. *Denton et al.* [2010] used the ion distributions of the plasma sheet boundary layer where plasma beta is of order unity to show the excitation of ion Bernstein waves which are predominantly electromagnetic. *Joyce et al.* [2012] suggested that waves observed in the solar wind could be interpreted as ion Bernstein waves in some cases, and *Boardsen et al.* [2015], using an instability analysis similar to *Denton et al.* [2010] and *Gary et al.* [2010] and through propagation of the ion Bernstein waves in a dipole field, suggested that compressional waves observed at Mercury could be interpreted as ion Bernstein waves. *Denton et al.* [2010] and *Gary et al.* [2010] further examined the dependence of the ion Bernstein instability on proton beta (β_p). At $\beta_p \ll 1$, the waves are predominantly electrostatic. At $\beta_p \sim 1$, the waves become electromagnetic and the fluctuating magnetic field has components in both the perpendicular and parallel directions, but the perpendicular fluctuations are larger. As β_p increases further beyond unity, the waves are still electromagnetic, but the magnetic field fluctuations become predominantly compressional, hence, resembling the fast magnetosonic waves observed in the inner magnetosphere.

Since several studies of local excitation [e.g., *Chen et al.*, 2010, 2011; *Xiao et al.*, 2013; *Ma et al.*, 2014] and propagation [e.g., *Boardsen et al.*, 1992; *Horne et al.*, 2000; *Xiao et al.*, 2013; *Zhou et al.*, 2014] of ion Bernstein waves in the inner magnetosphere assume the cold plasma magnetosonic dispersion relation for these waves, the earlier theoretical studies [*Perraut et al.*, 1982; *Denton et al.*, 2010; *Gary et al.*, 2010] raise the question of under what plasma condition the ion Bernstein waves approach the cold plasma magnetosonic dispersion relation and become "fast magnetosonic-like." *Liu et al.* [2011] first recognized the importance of this aspect and subsequently carried out fully electromagnetic particle-in-cell (PIC) simulations corresponding to two different plasma conditions representative of the plasma sheet boundary layer and the inner magnetosphere, respectively. They showed that a plasma entirely made of a single proton shell velocity distribution with a small shell speed of $v_s/v_A \approx 0.8$ excites ion Bernstein waves with phase speeds substantially less than the Alfvén speed. On the other hand, a plasma composed of a tenuous (10%) proton shell velocity distribution with a large shell speed ($v_s/v_A = 2$) and dense cold background protons excites ion Bernstein waves with phase speeds close to the Alfvén speed. This suggests that the excited waves are fast magnetosonic-like. For distinction, we shall describe the waves from the first case as "ion Bernstein-like."

The contrast between the two cases examined by *Liu et al.* [2011] suggests a "regime transition" of the instability, from being ion Bernstein-like to being fast magnetosonic-like or vice versa, associated with the changes of several key parameters of the shell velocity distribution, such as the relative concentration of the shell protons and the shell speed, effect of which has not been fully explored. *Min and Liu* [2015] recently developed a dispersion solver that accepts a sum of Maxwellian ring beam distributions (equation (2)) as a particle distribution and introduced a method to approximate a shell distribution with a finite series of the ring beam distributions. With the new tool in hand, the present study aims to reveal a more comprehensive picture of the regime transition of the ion Bernstein instability. In particular, we start from the general shell distribution introduced by *Liu et al.* [2011], vary the shell concentration and shell speed while others are fixed, and seek the parameter pairs that keep the maximum growth rates constant. The detailed description of the methodology is given in section 2, and the results are presented in section 3.

Throughout the paper, we denote the jth species plasma frequency as $\omega_j \equiv \sqrt{4\pi n_j e^2/m_j}$, the jth species cyclotron frequency as $\Omega_j \equiv e_j B_0/(m_j c)$, the jth component thermal speed as $\theta_j \equiv \sqrt{2T_j/m_j}$, and the jth component beta as $\beta_j \equiv 8\pi n_j T_j/B_0^2$. The Alfvén speed is $v_A \equiv B_0/\sqrt{4\pi n_0 m_p}$, the proton inertial length is $\lambda_p \equiv \sqrt{m_p c^2/4\pi n_0 e^2}$, and the lower hybrid frequency is $\omega_{\mathrm{lh}} = \omega_p/\sqrt{1+\omega_e^2/\Omega_e^2}$. Here n_0 is the unperturbed total plasma density, and B_0 denotes the uniform background magnetic field. As in *Liu et al.* [2011], a two-species plasma of protons (subscript p) and electrons (subscript e) is considered. Then the fully electromagnetic kinetic dispersion equation is numerically solved for the complex frequency $\omega = \omega_r + i\gamma$ at given pairs of wave normal angle ψ and wave number k, where $\gamma > 0$ indicates a growing fluctuation [*Min and Liu*, 2015].

Although not necessary, the same reduced proton-to-electron mass ratio of $m_p/m_e = 100$ and relatively small light-to-Alfvén speed ratio of $c/v_A = 15$ (equivalently $\omega_e/\Omega_e = 1.5$) as in *Liu et al.* [2011] are used throughout the paper. (The lower hybrid frequency is then $\omega_{\mathrm{lh}} \approx 8.3\Omega_p$.) With the realistic mass ratio and the typical value of $c/v_A \sim 400$ (or $\omega_e/\Omega_e \sim 10$) in the inner magnetosphere, there are potentially about 42 harmonic modes ($\omega_{\mathrm{lh}} \sim 42\Omega_p$) that can be simultaneously unstable. Finding numerical solutions of all harmonics is time consuming due to the increasing number of cyclotron order sums with the increasing harmonic frequency

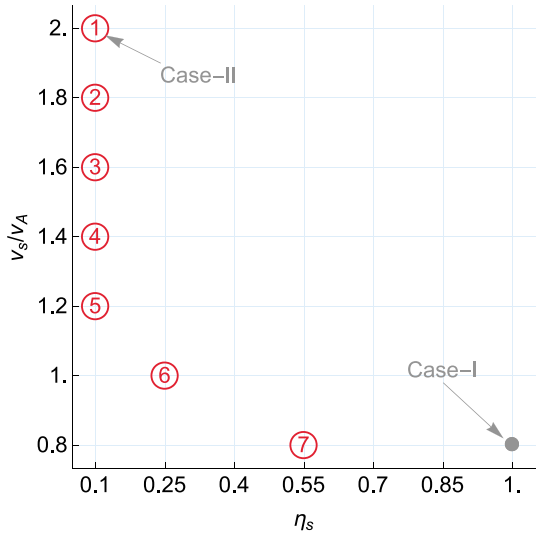

Figure 1. Schematic of the v_s-η_s space of the proton shell distribution models examined. Red-circled numbers denote locations of the (v_s, η_s) pairs resulting in $\gamma_m \sim 0.08\Omega_p$. "Case-I" and "Case-II" denote the shell parameters examined by *Liu et al.* [2011].

[e.g., *Gary et al.*, 2011] and numerous dispersion surfaces [e.g., *Min and Liu*, 2015, Figure 11] that should be identified and distinguished. While previous studies [*Denton et al.*, 2010; *Gary et al.*, 2010, 2011] focused on the first 10 or so harmonics, we instead cover all harmonics by effectively reducing the lower hybrid frequency. Although the detailed instability properties may vary with the choice of m_p/m_e and c/v_A, we expect that the main physics driving the regime transition will remain the same.

2. Methodology

The linear dispersion analyses in the present study use a two-component proton model of $f_p(\mathbf{v}) = f_M(v) + f_s(v)$, where $f_M(v)$ represents a Maxwellian thermal component and $f_s(v)$ represents an isotropic shell velocity distribution as a function of $v \equiv |\mathbf{v}| = \sqrt{v_\parallel^2 + v_\perp^2}$. The isotropic shell distribution [*Liu et al.*, 2011] is represented with

$$f_s(v) = \frac{\eta_s}{\pi^{3/2}\theta_s^3 C_s} e^{-(v-v_s)^2/\theta_s^2}, \tag{1}$$

where η_s, v_s and θ_s are the shell concentration, the shell speed, and the thermal spread of the shell, respectively, and $C_s = (2/\sqrt{\pi})(v_s/\theta_s)e^{-v_s^2/\theta_s^2} + (2v_s^2/\theta_s^2 + 1)(1 + \mathrm{erf}(v_s/\theta_s))$ is the normalization factor (here $\mathrm{erf}(x) \equiv (2/\sqrt{\pi})\int_0^x e^{-t^2}dt$). The Maxwellian distribution is represented with $f_M(v) = \eta_M e^{-v^2/\theta_M^2}/(\pi^{3/2}\theta_M^3)$. Note that η_s and η_M are the relative concentrations so $\eta_M + \eta_s = 1$. We choose $\theta_M/v_A = 0.045$ and $\theta_s/v_A = 0.45$ as fixed parameters, but $0.1 \le \eta_s \le 1$ and $0.8 \le v_s/v_A \le 2$ are left as free parameters (Figure 1). The upper and lower limits of η_s and v_s are determined from the two cases examined by *Liu et al.* [2011] (denoted as cases I and II in Figure 1). Electrons form a Maxwellian distribution with $T_e/T_M \approx 0.089$. Except for varying η_s and v_s, the parameters chosen are fully consistent with case II of *Liu et al.* [2011] (corresponding to model 1 in the present study).

For a given set of model parameters, the shell distribution of equation (1) is approximated with a finite series of ring beam distributions

$$f_r(v_\parallel, v_\perp) = \frac{\eta_r}{\pi^{3/2}\theta_\parallel\theta_\perp^2 C_r} e^{-(v_\parallel - v_d)^2/\theta_\parallel^2} e^{-(v_\perp - v_r)^2/\theta_\perp^2} \tag{2}$$

following the procedure described by *Min and Liu* [2015]. Here, v_d, $\theta_\parallel$, v_r, and $\theta_\perp$ are the drift speed, parallel thermal spread, ring speed, and perpendicular thermal spread, respectively, and $C_r = \exp(-v_r^2/\theta_\perp^2) + \sqrt{\pi}(v_r/\theta_\perp)\,\mathrm{erfc}(-v_r/\theta_\perp)$ is the normalization constant (here $\mathrm{erfc}(x) \equiv 1 - \mathrm{erf}(x)$). The number of ring beam components needed for convergence depends upon the v_s/θ_s ratio (but not on η_s). For the parameters considered here, we find that as few as 10 ring beam components for $v_s/v_A = 0.8$ and as many as 17 ring beam components for $v_s/v_A = 2$ are sufficient. We have rigorously verified the linear theory results against the results of several one-dimensional PIC simulations as in *Min and Liu* [2015] (supporting information).

As illustrated in Figure 1, the parameter space is discretized with v_s/v_A ranging from 0.8 to 2 in steps of 0.2 and η_s from 0.1 to 1 in steps of 0.15. *Min and Liu* [2015] showed that the maximum growth rate for model 1 is about $0.08\Omega_p$. Therefore, starting from model 1, we walk one step at a time toward the lower right corner in the η_s-v_s space and seek the model parameters that maintain the maximum growth rate of $\sim 0.08\Omega_p$. The locations of those parameters in the η_s-v_s space are numbered in sequence in Figure 1, and we will respectively label them as models 1, 2, etc. Hereafter, the linear theory results corresponding to these seven models at the wave normal angles that contain the most unstable harmonic mode are presented and discussed. From model 1 to model 7 these angles are, respectively, 88.4°, 88.5°, 88.5°, 88.75°, 89°, 88.8°, and 88.7°with an uncertainty of less than 0.2°(which is the wave normal angle step size used in the dispersion solver).

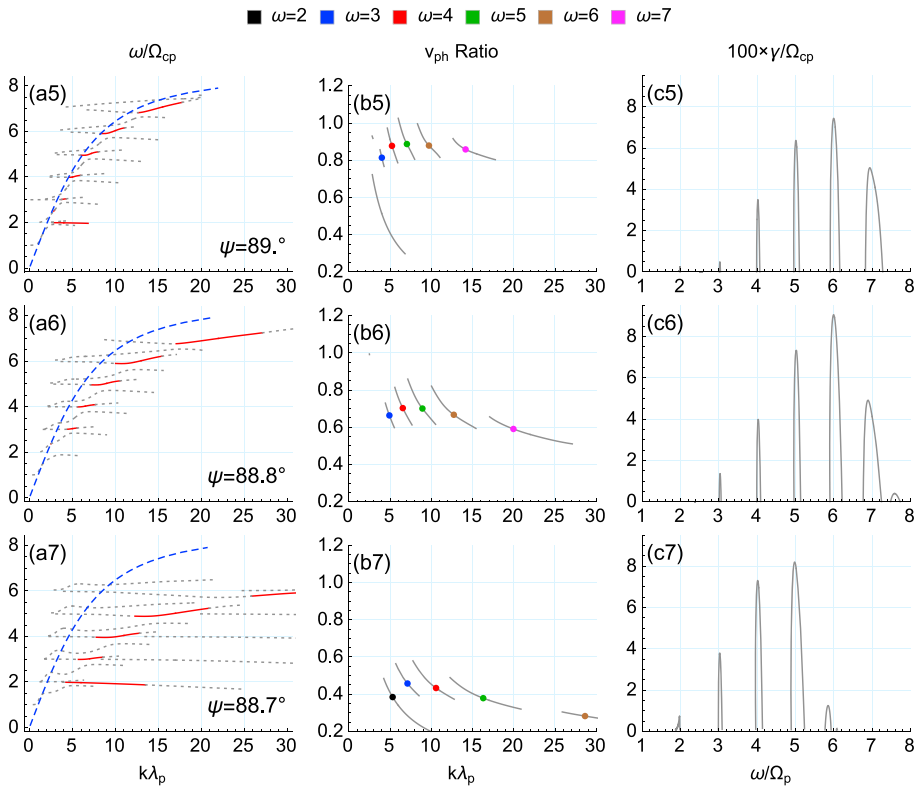

Figure 2. From top to bottom, linear theory results of models 5, 6, and 7, respectively. (left column) Linear theory dispersion relation. The red solid (gray dashed) curves correspond to growing (damping) modes, and the blue dashed curves correspond to the cold plasma dispersion relation for fast magnetosonic waves. The corresponding wave normal angle ψ is labeled at the bottom right corner. (middle column) Ratios of $v_{ph}/v_{ph,c}$ for the growing modes ($\gamma > 0$) as a function of $k\lambda_p$. The colored dots denote locations of the local growth rate peaks of the individual harmonic modes and the color represents harmonic number as labeled at the top. (right column) Linear growth rate as a function of real frequency.

3. Results

We first present the linear theory results that demonstrate the regime transition of the instability discussed in section 1. Figure 2 displays, from top to bottom, several properties of the instability corresponding to models 5, 6, and 7, respectively. The real frequency as a function of the wave number is shown in Figure 2 (left column), with the red solid (gray dashed) curves representing the $\gamma > 0$ ($\gamma < 0$) segments. For model 7, the unstable waves are far from the cold plasma magnetosonic dispersion curve (blue dashed curve) and clearly ion Bernstein waves. However, as the model parameters shift back toward model 5 (i.e., η_s decreases and v_s increases), the unstable waves gradually approach the cold plasma magnetosonic dispersion curve and become fast magnetosonic-like. This shift of the instability is quantitatively shown in Figure 2 (middle column) where the ratios of the phase speed of the unstable modes to the corresponding phase speed from the cold plasma magnetosonic dispersion relation ($v_{ph}/v_{ph,c}$) are plotted. The closer $v_{ph}/v_{ph,c}$ is to unity, the more fast magnetosonic-like the unstable waves are. For model 7, the ratios are below 0.5 for all harmonics, but for model 5, they are close to 0.9. Figure 2 (right column) demonstrates the harmonic nature of the instability in the real frequency space.

It may be more appropriate to investigate the properties of the instability at local growth rate maxima since the most unstable waves at each harmonic should eventually dominate over other modes. Figure 3 (top) shows from left to right the wave number, $v_{ph}/v_{ph,c}$ and growth rate as functions of model number for all seven proton distribution models shown in Figure 1. As in Figure 2 (middle column), the same colored dots are used to indicate the local growth rate peaks of the individual harmonic modes.

Figures 3a and 3b demonstrate the condition in which the regime transition occurs. When η_s is small (models 1 through 5; $\eta_s = 0.1$), wave growth occurs fairly close to the cold plasma magnetosonic dispersion relation

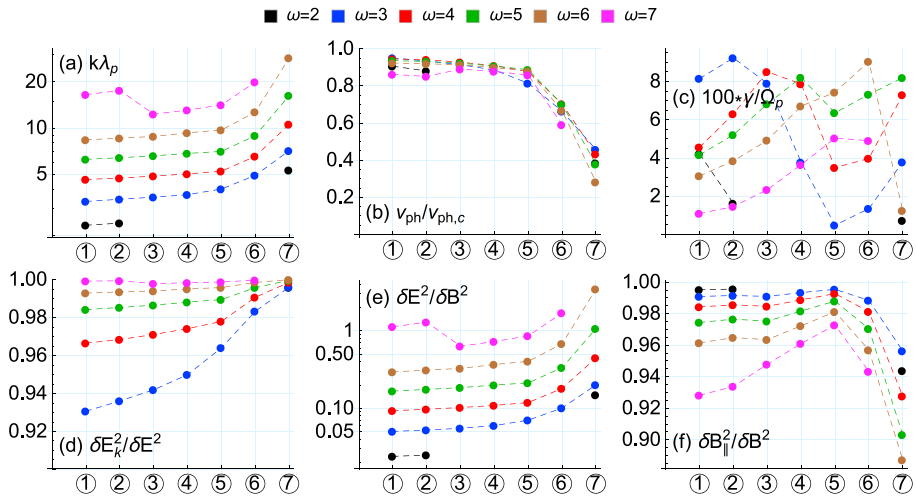

Figure 3. (top) Linear theory dispersion properties and (bottom) dimensionless ratios of various fluctuating fields at local growth rate maxima for all seven proton distribution models. Figure 3 (top) shows (a) $k\lambda_p$, (b) $v_{ph}/v_{ph,c}$, and (c) $100 \times \gamma/\Omega_p$, and Figure 3 (bottom) shows the ratios of (d) $|\delta E_{\mathbf{k}}|^2/|\delta E|^2$, (e) $|\delta E|^2/|\delta B|^2$, and (f) $|\delta B_{\parallel}|^2/|\delta B|^2$, as a function of model number. Colors differentiate individual harmonic modes as labeled at the top.

(i.e., $v_{ph}/v_{ph,c} \sim 1$), although the $v_{ph}/v_{ph,c}$ ratios decrease slightly with decreasing v_s. The unstable waves are therefore fast magnetosonic-like. However, the $v_{ph}/v_{ph,c}$ ratios fall sharply (or equivalently $k\lambda_p$ increases sharply) beyond model 5 when η_s starts to increase. So the unstable modes thereafter move away from the cold plasma magnetosonic dispersion relation and departs from being fast magnetosonic-like. It is worth emphasizing that the decrease of the phase speed with increasing η_s (and thereby increasing β_p) discussed above contradicts the behavior of the fast magnetosonic mode in magnetohydrodynamic theory for a thermal proton-electron plasma because the phase speed of the fast magnetosonic mode only increases with increasing β_p (more discussion in section 4). Figure 3c shows the local maximum instability growth rates as a function of model number. When v_s decreases while η_s is fixed to 0.1 (models 2 through 5), the harmonic number corresponding to the maximum growth rate increases, which is consistent with the previous theoretical analyses [e.g., *Horne et al.*, 2000; *Chen et al.*, 2010].

Linear dispersion theory also predicts dimensionless ratios of quadratic combinations of the various fluctuating field components of a specific mode [e.g., *Gary*, 1993, chapter 5]. Three of these ratios that further characterize the regime transition are shown in Figures 3d–3f as a function of model number for all seven proton distribution models examined. In all cases, the electric field fluctuations (Figure 3d) are predominantly electrostatic ($|\delta E_{\mathbf{k}}|^2/|\delta E|^2 > 0.92$) and the magnetic field fluctuations (Figure 3f) are predominantly compressional ($|\delta B_{\parallel}|^2/|\delta B|^2 > 0.88$). There are, however, subtle but nonnegligible changes. The $|\delta E_{\mathbf{k}}|^2/|\delta E|^2$ ratios approach unity with increasing harmonic number and, more interestingly, the ratios all converge very close to unity as the model parameters change from model 1 to model 7. The magnetic field fluctuations exhibit stronger compressional component for lower harmonic modes. As v_s/v_A decreases from 2 to 1.2 for fixed $\eta_s = 0.1$ (i.e., from model 1 to model 5), the $|\delta B_{\parallel}|^2/|\delta B|^2$ ratio remains relatively unchanged for lower harmonic modes but monotonically increases for higher harmonic modes. Then, the ratios all fall sharply as η_s increases from 0.1 to 0.55 for $v_s/v_A \sim 1$ (i.e., from model 5 to model 7). In contrast, the ratio of electric energy to magnetic energy (Figure 3e) varies in a broader range as a function of harmonic number ($0.01 < |\delta E|^2/|\delta B|^2 < 5$). The fluctuations become more electromagnetic (i.e., $|\delta E|^2/|\delta B|^2 \ll 1$) with decreasing harmonic number and, for individual harmonic modes, tend to become more electrostatic (i.e., $|\delta E|^2/|\delta B|^2 \gtrsim 1$) as the model parameters vary from model 1 to model 7. Again, the sharp transition occurs beyond model 5.

4. Conclusions and Discussion

The regime transition of the ion Bernstein instability from being ion Bernstein-like to being fast magnetosonic-like is studied using linear kinetic dispersion theory. The positive slopes of the proton velocity distribution with respect to the perpendicular (to the background magnetic field) velocity ($\partial f_p/\partial v_\perp > 0$) are modeled with an isotropic shell velocity distribution. Then the properties of unstable waves are obtained by

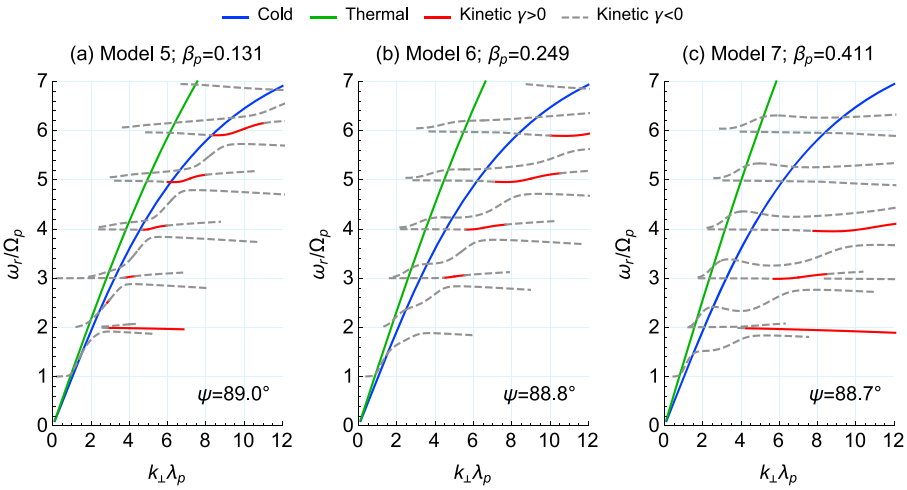

Figure 4. Comparison of the fully kinetic dispersion relation (red solid and gray dashed curves) with the thermal (green curves) and cold (blue curves) fast magnetosonic wave dispersion relations in magnetohydrodynamic theory. (a)–(c) Models 5–7, respectively, at specific wave normal angles as labeled. Note that the fully kinetic and cold fast magnetosonic wave dispersion relations are identical to Figure 2 (left column).

numerically solving the full kinetic dispersion relation for the complex frequency given the real wave number and wave normal angle. While having the thermal spread of the proton shell distributions fixed, the shell concentration and the shell speed are varied, and pairs of those parameters resulting in the constant maximum growth rate are sought. The results clearly demonstrate the regime transition of the instability as the shell concentration varies. When the shell concentration becomes less than 10%, the dispersion relations of the unstable waves, which are essentially ion Bernstein waves, approach the cold plasma dispersion relation for fast magnetosonic waves. Although the shell velocity also changes the dispersion properties of the unstable waves, its influence on the regime transition of the instability is minor.

The phase speed decrease of the unstable waves with increasing η_s as demonstrated by Figure 2 clearly contradicts the behavior of the fast magnetosonic mode in magnetohydrodynamic theory. To show this, we solve the low-frequency dispersion relation (LFDR) derived from the linearized fluid equations for a thermal proton-electron plasma [*Swanson*, 2003, p. 90]:

$$\left(1-\frac{\omega^2}{k^2v_A^2}-\frac{\omega^2}{|\Omega_e|\Omega_p}+\frac{k^2c_s^2\sin^2\psi}{\omega^2-k^2c_s^2}\right)\left(\cos^2\psi-\frac{\omega^2}{k^2v_A^2}-\frac{\omega^2}{|\Omega_e|\Omega_p}\right)=\frac{\omega^2\cos^2\psi}{\Omega_p^2}, \tag{3}$$

where $c_s\equiv\sqrt{(\gamma_eT_e+\gamma_pT_p)/(m_e+m_p)}$ is the ion acoustic speed and γ_j is the ratio of specific heats for species j. The fast magnetosonic mode corresponds to the solution with the largest phase speed. Since in the present paper $T_e/T_p \ll 1$ is assumed, $c_s^2/v_A^2 \simeq \gamma_p\beta_p$. With $\gamma_p = 5/3$, Figures 4a–4c display the fast magnetosonic mode solutions of LFDR (green curves) for models 5–7, respectively. While it is difficult to precisely define β_p of the two-component proton model, here it is obtained simply from the effective temperature of the shell $3T_s/m_p = \int_0^\infty 4\pi v^4 f_s(v)\mathrm{d}v$, and thus $\beta_p = 2((1-\eta_s)T_M+\eta_sT_s)/(m_pv_A^2)$. Accordingly, proton betas for the three models are $\beta_p \approx 0.13$, 0.25, and 0.41, respectively. For comparison, the solutions of the cold plasma dispersion relation (blue curves) and the full kinetic dispersion relation (gray dashed and red solid curves) from Figure 2 (left column) are also plotted. The apparent difference between the dispersion relation of the unstable waves (red curves) and the thermal fast magnetosonic wave dispersion relation (green curves) further confirms that these waves are essentially ion Bernstein waves. Only when the shell proton concentration becomes sufficiently small (less than 10%), do the unstable waves approach the cold plasma dispersion relation for fast magnetosonic waves and become fast magnetosonic-like.

Finally, recent studies suggest that fast magnetosonic waves (i.e., equatorial noise) in the inner magnetosphere can substantially affect dynamics of radiation belt electrons via resonant and nonresonant interactions with the waves [*Horne et al.*, 2007; *Bortnik and Thorne*, 2010; *Shprits*, 2009] and have since received growing attention. Statistical studies [*Meredith et al.*, 2008; *Ma et al.*, 2013] show that these waves can occur in and/or reach up to $L \approx 8$ with substantial occurrence rates even though they are concentrated in $L \lesssim 6$. Interestingly,

average intensity of the waves occurring outside of the plasmapause is larger than those within the plasmasphere [*Ma et al.*, 2013], indicating that the waves occurring in a plasma with a less dense cold background can have more significant effect on the radiation belt electrons. Considering the sizable proportion of the events outside of the plasmapause, our results as well as previous studies [*Denton et al.*, 2010; *Gary et al.*, 2010; *Liu et al.*, 2011] suggest that one should be more cautious in assuming the cold plasma dispersion relation for fast magnetosonic waves throughout the inner magnetosphere.

Acknowledgments
Data supporting the figures presented are available upon request from the lead author. The work at Auburn University was supported by NASA grant NNX13AD62G and NSF grant 1303623. Authors thank S. Peter Gary for fruitful discussions.

Michael Balikhin thanks Scott Boardsen and Yuri Shprits for their assistance in evaluating this paper.

References

Balikhin, M. A., Y. Y. Shprits, S. N. Walker, L. Chen, N. Cornilleau-Wehrlin, I. Dandouras, O. Santolik, C. Carr, K. H. Yearby, and B. Weiss (2015), Observations of discrete harmonics emerging from equatorial noise, *Nat. Commun.*, *6*, 7703, doi:10.1038/ncomms8703.

Boardsen, S. A., D. L. Gallagher, D. A. Gurnett, W. K. Peterson, and J. L. Green (1992), Funnel-shaped, low-frequency equatorial waves, *J. Geophys. Res.*, *97*(A10), 14,967–14,976, doi:10.1029/92JA00827.

Boardsen, S. A., E.-H. Kim, J. M. Raines, J. A. Slavin, D. J. Gershman, B. J. Anderson, H. Korth, T. Sundberg, D. Schriver, and P. Travnicek (2015), Interpreting ~1 Hz magnetic compressional waves in Mercury's inner magnetosphere in terms of propagating ion-Bernstein waves, *J. Geophys. Res. Space Physics*, *120*, 4213–4228, doi:10.1002/2014JA020910.

Bortnik, J., and R. M. Thorne (2010), Transit time scattering of energetic electrons due to equatorially confined magnetosonic waves, *J. Geophys. Res.*, *115*, A07213, doi:10.1029/2010JA015283.

Chen, L. (2015), Wave normal angle and frequency characteristics of magnetosonic wave linear instability, *Geophys. Res. Lett.*, *42*, 4709–4715, doi:10.1002/2015GL064237.

Chen, L., R. M. Thorne, V. K. Jordanova, and R. B. Horne (2010), Global simulation of magnetosonic wave instability in the storm time magnetosphere, *J. Geophys. Res.*, *115*, A11222, doi:10.1029/2010JA015707.

Chen, L., R. M. Thorne, V. K. Jordanova, M. F. Thomsen, and R. B. Horne (2011), Magnetosonic wave instability analysis for proton ring distributions observed by the LANL magnetospheric plasma analyzer, *J. Geophys. Res.*, *116*, A03223, doi:10.1029/2010JA016068.

Denton, R. E., M. J. Engebretson, A. Keiling, A. P. Walsh, S. P. Gary, P. M. E. Décréau, C. A. Cattell, and H. Rème (2010), Multiple harmonic ULF waves in the plasma sheet boundary layer: Instability analysis, *J. Geophys. Res.*, *115*, A12224, doi:10.1029/2010JA015928.

Gary, S. P. (1993), *Theory of Space Plasma Microinstabilities*, Cambridge Univ. Press, New York.

Gary, S. P., K. Liu, D. Winske, and R. E. Denton (2010), Ion Bernstein instability in the terrestrial magnetosphere: Linear dispersion theory, *J. Geophys. Res.*, *115*, A12209, doi:10.1029/2010JA015965.

Gary, S. P., K. Liu, and D. Winske (2011), Bernstein instability driven by suprathermal protons in the ring current, *J. Geophys. Res.*, *116*, A08215, doi:10.1029/2011JA016543.

Gul'elmi, A., B. Klaine, and A. Potapov (1975), Excitation of magnetosonic waves with discrete spectrum in the equatorial vicinity of the plasmapause, *Planet. Space Sci.*, *23*(2), 279–286, doi:10.1016/0032-0633(75)90133-6.

Horne, R. B., G. V. Wheeler, and H. S. C. K. Alleyne (2000), Proton and electron heating by radially propagating fast magnetosonic waves, *J. Geophys. Res.*, *105*(A12), 27,597–27,610, doi:10.1029/2000JA000018.

Horne, R. B., R. M. Thorne, S. A. Glauert, N. P. Meredith, D. Pokhotelov, and O. Santolík (2007), Electron acceleration in the Van Allen radiation belts by fast magnetosonic waves, *Geophys. Res. Lett.*, *34*, L17107, doi:10.1029/2007GL030267.

Janhunen, P., A. Olsson, A. Vaivads, and W. K. Peterson (2003), Generation of Bernstein waves by ion shell distributions in the auroral region, *Ann. Geophys.*, *21*(4), 881–891, doi:10.5194/angeo-21-881-2003.

Joyce, C. J., C. W. Smith, P. A. Isenberg, S. P. Gary, N. Murphy, P. C. Gray, and L. F. Burlaga (2012), Observation of Bernstein waves excited by newborn interstellar pickup ions in the solar wind, *Astrophys. J.*, *745*(2), 112, doi:10.1088/0004-637X/745/2/112.

Liu, K., S. P. Gary, and D. Winske (2011), Excitation of magnetosonic waves in the terrestrial magnetosphere: Particle-in-cell simulations, *J. Geophys. Res.*, *116*, A07212, doi:10.1029/2010JA016372.

Ma, Q., W. Li, R. M. Thorne, and V. Angelopoulos (2013), Global distribution of equatorial magnetosonic waves observed by THEMIS, *Geophys. Res. Lett.*, *40*, 1895–1901, doi:10.1002/grl.50434.

Ma, Q., W. Li, L. Chen, R. M. Thorne, and V. Angelopoulos (2014), Magnetosonic wave excitation by ion ring distributions in the Earth's inner magnetosphere, *J. Geophys. Res. Space Physics*, *119*, 844–852, doi:10.1002/2013JA019591.

McClements, K. G., R. O. Dendy, and C. N. Lashmore-Davies (1994), A model for the generation of obliquely propagating ULF waves near the magnetic equator, *J. Geophys. Res.*, *99*(A12), 23,685–23,693, doi:10.1029/94JA01979.

Meredith, N. P., R. B. Horne, and R. R. Anderson (2008), Survey of magnetosonic waves and proton ring distributions in the Earth's inner magnetosphere, *J. Geophys. Res.*, *113*, A06213, doi:10.1029/2007JA012975.

Min, K., and K. Liu (2015), Fast magnetosonic waves driven by shell velocity distributions, *J. Geophys. Res. Space Physics*, *120*, 2739–2753, doi:10.1002/2015JA021041.

Perraut, S., A. Roux, P. Robert, R. Gendrin, J.-A. Sauvaud, J.-M. Bosqued, G. Kremser, and A. Korth (1982), A systematic study of ULF waves above f_{H+} from GEOS 1 and 2 measurements and their relationships with proton ring distributions, *J. Geophys. Res.*, *87*(A8), 6219–6236, doi:10.1029/JA087iA08p06219.

Russell, C. T., R. E. Holzer, and E. J. Smith (1970), OGO 3 observations of ELF noise in the magnetosphere: 2. The nature of the equatorial noise, *J. Geophys. Res.*, *75*(4), 755–768, doi:10.1029/JA075i004p00755.

Santolík, O., J. S. Pickett, D. A. Gurnett, M. Maksimovic, and N. Cornilleau-Wehrlin (2002), Spatiotemporal variability and propagation of equatorial noise observed by Cluster, *J. Geophys. Res.*, *107*(A12), 1495, doi:10.1029/2001JA009159.

Shprits, Y. Y. (2009), Potential waves for pitch-angle scattering of near-equatorially mirroring energetic electrons due to the violation of the second adiabatic invariant, *Geophys. Res. Lett.*, *36*, L12106, doi:10.1029/2009GL038322.

Swanson, D. (2003), *Plasma Waves*, 2nd ed., Series in Plasma Physics and Fluid Dynamics, Taylor and Francis, New York.

Thomsen, M. F., M. H. Denton, V. K. Jordanova, L. Chen, and R. M. Thorne (2011), Free energy to drive equatorial magnetosonic wave instability at geosynchronous orbit, *J. Geophys. Res.*, *116*, A08220, doi:10.1029/2011JA016644.

Xiao, F., Q. Zhou, Z. He, C. Yang, Y. He, and L. Tang (2013), Magnetosonic wave instability by proton ring distributions: Simultaneous data and modeling, *J. Geophys. Res. Space Physics*, *118*, 4053–4058, doi:10.1002/jgra.50401.

Zhou, Q., et al. (2014), Excitation of nightside magnetosonic waves observed by Van Allen Probes, *J. Geophys. Res. Space Physics*, *119*, 9125–9133, doi:10.1002/2014JA020481.